

Electronic Structures across the Superconductor-Insulator Transition at $\text{La}_{2.85}\text{Pr}_{0.15}\text{Ni}_2\text{O}_7/\text{SrLaAlO}_4$ Interfaces

Heng Wang^{1†}, Haoliang Huang^{1,2†*}, Guangdi Zhou^{1†}, Wei Lv¹, Changming Yue^{1,2,3}, Lizhi Xu¹,
Xianfeng Wu¹, Zihao Nie¹, Yaqi Chen¹, Yu-Jie Sun^{1,2}, Weiqiang Chen^{1,2}, Hongtao Yuan⁴, Zhuoyu
Chen^{1,2*}, Qi-Kun Xue^{1,2,5*}

¹*Department of Physics and Guangdong Basic Research Center of Excellence for Quantum
Science, Southern University of Science and Technology, Shenzhen 518055, China*

²*Quantum Science Center of Guangdong-Hong Kong-Macao Greater Bay Area, Shenzhen
518045, China*

³*Guangdong Provincial Key Laboratory of Advanced Thermoelectric Materials and Device
Physics, Southern University of Science and Technology, Shenzhen, 518055, China*

⁴*National Laboratory of Solid State Microstructures, College of Engineering and Applied
Sciences, Nanjing University, Nanjing, China.*

⁵*Department of Physics, Tsinghua University, Beijing 100084, China*

ABSTRACT:

Interfacial superconductivity discovered in bilayer nickelate heterostructures opens new avenues for effective tunability and control. Here, we report the superconductor-insulator transition in $\text{La}_{2.85}\text{Pr}_{0.15}\text{Ni}_2\text{O}_7/\text{SrLaAlO}_4$ interfaces, with corresponding electronic structures revealed using synchrotron low-temperature X-ray absorption spectroscopy (XAS) and X-ray linear dichroism (XLD). In addition to the valence states of each element within the films determined by XAS, XLD at the O K edge pre-peak reveals hybridizations involving both $2p_z$ and $2p_x/2p_y$ orbitals, which are concomitantly suppressed upon oxygen loss. Intriguingly, such oxygen loss that eliminates superconductivity, induces a qualitative XLD change at the Ni L_2 edge, implying significant transformations among $3d_{x^2-y^2}$ and $3d_{z^2}$ energy bands near the Fermi level. Our findings establish an element- and orbital-resolved electronic framework for the origin of superconductivity.

The Ruddlesden-Popper (RP) nickelates have emerged as a new class of high-transition temperature (T_C) superconductors, both under high pressure [1-5] and at ambient pressure [6-8]. Structurally, RP nickelates feature covalently bonded apical oxygens that couple adjacent Ni-O layers [7, 9-11], which is distinct from cuprates and iron-based superconductors, suggesting key roles of Ni $3d_{z^2}$ and O $2p_z$ orbitals [12-16]. From an electronic structure perspective, RP nickelates, particularly the bilayer systems, exhibit Fermi surfaces involving both $3d_{x^2-y^2}$ and $3d_{z^2}$ orbitals [10,17], in contrast to the single-band scenario seen in the cuprates [18], and more closely resembling the situation in iron-based superconductors [19].

Interfacial superconductivity, arising from couplings across heterostructures [20-25], often offers enhanced tunability at reduced dimensionality [26,27]. Such tunability facilitates the realization of superconductor-insulator transitions (SIT) [28-34], providing an effective approach for exploring superconducting phase diagrams. In oxide superconductors, tuning the oxygen content has proven to be an effective method to fine control SIT [35]. The recently discovered interfacial superconductivity in bilayer nickelate heterostructures are found to be highly sensitive to oxygen deficiency [6-8,17], offering opportunities to explore this new class of high- T_C superconductors with oxygen content tunability.

Probing the electronic structure change across the superconductor to non-superconductor transitions, is crucial for understanding the origin of

superconductivity [18]. Unlike photoemission that probes occupied states [17], X-ray absorption spectroscopy (XAS) accesses unoccupied states above the Fermi level (E_F) with elemental selectivity, while its polarization-dependent extension—X-ray linear dichroism (XLD)—may further resolve orbitals [36-39]. These techniques have been instrumental in studying cuprate, iron-based, and infinite-layer nickelate superconductors [40-44]. Here, we employ XAS and XLD to characterize electronic structure evolutions across the oxygen content-tuned SIT phase diagram of the $\text{La}_{2.85}\text{Pr}_{0.15}\text{Ni}_2\text{O}_7/\text{SrLaAlO}_4$ heterointerface.

Shown in Fig. 1(a) is a scanning transmission electron microscopy (STEM) image of a superconducting $\text{La}_{2.85}\text{Pr}_{0.15}\text{Ni}_2\text{O}_7$ (LPNO)/ SrLaAlO_4 (SLAO) heterostructure, prepared using gigantic-oxidative atomic-layer-by-layer epitaxy (GOALL-Epitaxy) [7,45]. The superconductivity is localized near the interface between the three-unit-cell pure-phase LPNO film and the treated SLAO substrate, as schematically illustrated in Fig. 1(a) [17]. XAS of the four constituent elements (namely La, Pr, Ni, O) in the film are shown in Fig. 1(b)-1(e) ([46] Fig. S1 show the XAS of another superconducting sample and an insulating bilayer nickelate thin film for reference). By comparing the M_4 and M_5 peaks to those of reference compounds, we confirm that both La and Pr exhibit +3 valence states. The Ni L_3 peaks overlap with the tail of the La M_4 peak, complicating accurate analysis. Therefore, we exclude the L_3 features from further discussion. The Ni L_2 peak of

the LPNO sample is positioned between those of NiO and $\text{Nd}_{0.8}\text{Sr}_{0.2}\text{NiO}_3$, indicating that Ni adopts an average valence state between +2 and +3. Note that finite Sr atoms diffuse from the substrate into the film, and cause hole-doping for the observed superconductivity. The Ni valence near the interface may be modestly higher than that in regions closer to the top surface. A pre-peak is apparently observed at energies prior to the O K edge, signifying the presence of oxygen $2p$ states near the Fermi level. These O $2p$ states hybridize with the Ni $3d$ states, forming the Fermi surfaces from which superconductivity develops.

Superconductivity in the LPNO/SLAO heterostructure is highly sensitive to oxygen content [6-8]. By *in situ* fine tuning oxygen content inside the transport measurement cryostat (as detailed in Methods [46]), the superconductor-insulator transition is demonstrated in Fig. 2(a). The resistivity-temperature (R - T) curve for the highest oxygen content case exhibits a two-step resistive drop, previously observed in disordered two-dimensional/interfacial superconductors described by Josephson-coupled superconducting puddles with phase fluctuations [31,35,47]. As oxygen content decreases, the resistivity at 200 K increases, accompanied by a deterioration of the superconducting property, although a resistive drop from Cooper pair conduction persists. When oxygen content is further reduced, the R - T curves exhibit metal-insulator transitions occurring at progressively elevated temperatures. The oxygen content is quantified via the empirical relation $p =$

557/ $R(200\text{ K})$, with the oxygen content of the initial state set to 1 (Similar results were also observed for another LPNO superconducting sample in Fig. S3. [46]), following prior conventions [35,48]. Consistent with a picture of continuous two-dimensional quantum phase transitions, resistivity around the SIT can be scaled and collapses to be a single function of $u = |p - p_c|T^{-1/z\nu}$ (Fig. 2(a) inset). An exponent of $z\nu = 2.3$ optimally scales the data, closely matching the theoretical value of $7/3$ for a quantum percolation model. In this framework, the SIT is driven by the decoupling of localized superconducting puddles due to suppressed Josephson coupling in a disordered two-dimensional system. The observed two-step R - T features align with this interpretation. The critical resistance here is about $0.67\text{ k}\Omega$ (see Fig. S2 [46]), significantly lower than the value $h/(4e^2)$ anticipated for the a purely bosonic model [30], resembling observations in other interfacial superconductors [27-29,31,33]. Resistivity and its temperature derivative (dR/dT) are plotted as color-mapped intensities within temperature–oxygen content phase diagrams, enabling direct visualization of the SIT, as shown in Fig. 2(b) and 2(c).

To probe the electronic structure evolution across the SIT, we conducted synchrotron XAS and XLD measurements. The ultra-high vacuum (UHV) endstation is equipped with a temperature-controlled sample manipulator (15 K-400 K), enabling oxygen content modulation at elevated temperatures (e.g. 350 K) and stabilization of oxygen content at cryogenic conditions (e.g. 100 K) [49]. We

first investigate the influence of oxygen deficiency on the oxygen $2p$ states near E_F . Under UHV conditions with the temperature stabilized at 350 K, oxygen content in the superconducting LPNO/SLAO sample was gradually reduced. Corresponding XAS spectra reveal a systematic evolution of the O K -edge pre-peak intensity, as displayed in Fig. 3(a). As the system transitions from a superconducting to an insulating state, the integrated area of the O K edge pre-peak (Fig. 3(a), inset) progressively diminishes, reflecting suppressed hybridization between oxygen $2p$ orbitals and states near E_F .

To resolve the orbital anisotropy of oxygen $2p$ states, we performed polarization-dependent XLD measurements at 100 K for a superconducting case (Fig. 3(b)) and an insulating case (Fig. 3(c)). By varying the incident photon polarization angle, we extracted the in-plane (I_{ab}) and out-of-plane (I_c) absorption intensities (see Methods [46]), which selectively probe the oxygen $2p_x/2p_y$ and $2p_z$ orbitals, respectively. This selectivity stems from linearly polarized X-rays preferentially excite orbitals aligned with the electric field vector (Fig. 3(d), schematic). For the superconducting sample, both I_{ab} and I_c exhibit non-zero spectral weight at the O K pre-peak (Fig. 3(b)), indicating contributions from all three $2p$ orbitals near E_F . Notably, the I_c peak is weaker and shifted to lower energy relative to I_{ab} , reflecting distinct energy distributions of $2p_z$ versus $2p_x/2p_y$ states (Fig. 3(e)). In contrast, the oxygen-deficient insulating sample show a pronounced

suppression of both I_{ab} and I_c (Fig. 3(b)), demonstrating that oxygen loss uniformly diminishes the $2p_z$ and $2p_x/2p_y$ orbital hybridizations.

XLD analysis at the Ni L_2 edge reveals stark orbital contrast between superconducting (Fig. 4(a)) and insulating (Fig. 4(b)) states. In the Ni-O octahedral coordination, the out-of-plane $3d_{z^2}$ orbital couples selectively to I_c (out-of-plane polarization), while the in-plane $3d_{x^2-y^2}$ dominates I_{ab} (in-plane polarization). In the superconducting state (Fig. 4(a)), the finite magnitude of both I_{ab} and I_c indicate the coexistence of $3d_{x^2-y^2}$ and $3d_{z^2}$ states near E_F . The dominant I_{ab} intensity and its extended high-energy tail reflect a higher density of unoccupied $3d_{x^2-y^2}$ states near E_F . This aligns with angle-resolved photoemission spectroscopy (ARPES) measurements of the occupied states [17] and the associated DFT+cRPA+DMFT analysis [10], where interlayer hopping t_c splits the $3d_{z^2}$ band into a near-full occupied bonding band and an antibonding band, leaving $3d_{x^2-y^2}$ as the primary contributor to unoccupied state above E_F , due to the larger in-plane bandwidth dominated by strong in-plane hopping t_{ab} (Fig. 4(c)). This scenario is also consistent with the observation in O K edge pre-peak in Fig. 3, as oxygen $2p_z$ and $2p_x/2p_y$ strongly hybridize with $3d_{z^2}$ and $3d_{x^2-y^2}$, respectively. The same conclusion can be drawn from another LPNO superconducting film as shown in Fig. S4 [46]. In contrast, oxygen-deficient insulating samples show a marked reversal: I_c dominates at lower energies, surpassing I_{ab} , while I_{ab} persists to higher energies

(Fig. 4(b)). This orbital reconfiguration is far beyond a rigid band shift (Fig. 4(d)), which may directly link to the collapse of superconductivity.

The O K edge pre-peak in RP nickelates exhibits both similarities and distinctions compared to cuprates. In cuprates, the fully occupied $3d_{z^2}$ and $2p_z$ orbitals lie far below E_F , leaving the hybridized in-plane oxygen $2p_x/2p_y$ and Cu $3d_{x^2-y^2}$ orbitals to dominate the low-energy electronic structures, consistent with their charge-transfer insulating nature. This strong $2p$ - $3d$ hybridization can lead to augmented electron-phonon coupling, in which oxygen-derived phonons may enhanced pairing interactions [50]. In contrast, RP nickelates display pre-peak contributions from all three oxygen $2p$ orbitals—a feature absent in cuprates. This suggests a distinct mechanism for superconductivity, where interlayer hopping t_c and apical oxygen play pivotal roles. Notably, infinite-layer nickelates, despite structural similarities to cuprates, lack the O K -edge pre-peak due to their Mott-Hubbard character [42,43], where oxygen $2p$ hybridization near E_F diminishes. Their suppressed T_C compared to cuprates again hints at a possible link between strong $2p$ - $3d$ hybridization and enhanced pairing strength.

In cuprate superconductors, oxygen content variations mainly occur within the charge reservoir layers, preserving the structural integrity of the superconducting Cu-O planes and allowing charge doping dominating the electronic response. In marked contrast, RP nickelate exhibit the oxygen

deficiencies located both at the apical sites and in the Ni-O planes (as revealed in Fig. 3), each disrupting superconductivity through distinct mechanisms. Apical oxygen vacancies substantially alter the interlayer hopping t_c that transforms orbital configurations near E_F and may introduce local moments [51,52]. In-plane oxygen loss, on the other hand, directly perturbs the Ni-O bonding network critical for charge transport. Both types of oxygen vacancy induce disorders in the system, leading to the insulating behavior.

In summary, utilizing polarization-dependent X-ray absorption spectroscopy, we elucidated the element- and orbital-resolved electronic structure evolution across the superconductor-insulator transition in the $\text{La}_{2.85}\text{Pr}_{0.15}\text{Ni}_2\text{O}_7/\text{SrLaAlO}_4$ heterostructure. In the superconducting state, we reveal the coexistence of Ni $3d_{x^2-y^2}$ and $3d_{z^2}$ orbitals near E_F , alongside contributions from O $2p_x$, $2p_y$, and $2p_z$, with $3d_{z^2}/2p_z$ states being subdominant. Upon the destruction of superconductivity by oxygen deficiency, while all oxygen $2p$ states exhibit suppressions, the $3d_{z^2}$ associated absorption intensity increase markedly, even surpassing the $3d_{x^2-y^2}$ associated intensity at lower energies, implying $3d_{z^2}$ states gain dominance over $3d_{x^2-y^2}$ at energies closer to E_F . Our results unambiguously demonstrate the multi-orbital nature of the superconducting electronic states near E_F , emphasizing the critical role of z -axis orbitals. The oxygen-deficient state triggers a drastic electronic reconstruction that directly correlates with the loss of superconductivity.

This work establishes a foundational link between electronic orbitals and superconductivity in bilayer nickelates, highlights the potential of orbital-specific engineering in nickelate heterostructures, offering new pathways to tailor and enhance superconducting properties.

Acknowledgments -This work was supported by the National Key R&D Program of China (2024YFA1408101 and 2022YFA1403101), the Natural Science Foundation of China (92265112, 12374455, 52388201, 92365203, 52072168, & U24A6002), the Guangdong Provincial Quantum Science Strategic Initiative (GDZX2401004 & GDZX2201001), the Shenzhen Science and Technology Program (KQTD20240729102026004), and the Shenzhen Municipal Funding Co-Construction Program Project (SZZX2301004 & SZZX2401001). H.W. acknowledges the support by the China Postdoctoral Science Foundation (GZB20240294 & 2024M751287).

Data availability - The data that support the findings of this study are presented in the Article and its Supplementary Materials. Further data are available from the corresponding authors upon reasonable request.

†These authors contributed equally.

*Corresponding author. E-mail: chenzhuoyu@sustech.edu.cn (Z.C.),
huanghaoliang@quantumsc.cn (H.H.), xueqk@sustech.edu.cn (Q.K.X.)

- [1] H. Sun *et al.*, Nature **621**, 493 (2023).
- [2] J. Hou *et al.*, Chin. Phys. Lett. **40**, 117302 (2023).
- [3] Y. Zhang *et al.*, Nat. Phys. **20**, 1269 (2024).
- [4] G. Wang *et al.*, Phys. Rev. X **14**, 011040 (2024).
- [5] N. Wang *et al.*, Nature **634**, 579 (2024).
- [6] E. K. Ko *et al.*, Nature doi: 10.1038/s41586-024-08525-3 (2024).
- [7] G. Zhou *et al.*, arXiv:2412.16622 (2024).
- [8] Y. Liu *et al.*, arXiv:2501.08022 (2025)
- [9] Z. Dong *et al.*, Nature **630**, 847 (2024).
- [10] C. Yue *et al.*, arXiv:2501.06875 (2025).
- [11] L. Bhatt *et al.*, arXiv:2501.08204 (2025).
- [12] Z. Luo *et al.*, Phys. Rev. Lett. **131**, 126001 (2023).
- [13] X. Chen *et al.*, Nat. Commun. **15**, 9597 (2024).
- [14] C. Lu *et al.*, Phys. Rev. Lett. **132**, 146002 (2024).
- [15] C. Lu *et al.*, Phys. Rev. B **110**, 094509 (2024).
- [16] J. Yang *et al.*, Nat. Commun. **15**, 4373 (2024).
- [17] P. Li *et al.*, arXiv:2501.09255 (2025).
- [18] B. Keimer *et al.*, Nature **518**, 179 (2015).

- [19] X. Chen *et al.*, Nat. Sci. Rev. **1**, 371 (2014).
- [20] H. Y. Hwang *et al.*, Nat. Mater. **11**, 103 (2012).
- [21] A. Ohtomo & H. Y. Hwang, Nature **427**, 423 (2004).
- [22] N. Reyren *et al.*, Science **317**, 1196 (2007).
- [23] A. Gozar *et al.*, Nature **455**, 782 (2008).
- [24] Q.-Y. Wang *et al.*, Chin. Phys. Lett. **29**, 037402 (2012).
- [25] J. J. Lee *et al.*, Nature **515**, 245 (2014).
- [26] J. Mannhart & D. G. Schlom, Science **327**, 1607 (2010).
- [27] Y. Saito *et al.*, Nat. Rev. Mater. **2**, 16094 (2017).
- [28] A. D. Caviglia *et al.*, Nature **456**, 624 (2008).
- [29] C. Bell *et al.*, Phys. Rev. Lett. **103**, 226802 (2009).
- [30] A. T. Bollinger *et al.*, Nature **472**, 458 (2011).
- [31] Z. Chen *et al.*, Nat. Commun. **9**, 4008 (2018).
- [32] C. Yang *et al.*, Science **366**, 1505 (2019).
- [33] Z. Chen *et al.*, Science **372**, 721 (2021).
- [34] B. D. Faeth *et al.*, Phys. Rev. X **11**, 021054 (2021).
- [35] Y. Yu *et al.*, Nature **575**, 156 (2019).
- [36] E. Benckiser *et al.*, Nat. Mater. **10**, 189 (2011).
- [37] Z. Liao *et al.*, Nat. Commun. **10**, 589 (2019).
- [38] J. Zhang *et al.*, Nat. Phys. **13**, 864 (2017).

- [39] X. Ren *et al.*, Commun. Phys. **8**, 52 (2025).
- [40] J. M. Tranquada *et al.*, Phys. Rev. B **36**, 5263 (1987).
- [41] F. Bondino *et al.*, Phys. Rev. Lett. **101**, 267001 (2008).
- [42] M. Hepting *et al.*, Nat. Mater. **19**, 381 (2020).
- [43] Z. Chen *et al.*, Matter **5**, 1806 (2022).
- [44] S. Zeng *et al.*, Phys. Rev. Lett. **133**, 066503 (2024).
- [45] G. Zhou *et al.*, Natl. Sci. Rev. nwae429 (2024).
- [46] See Supplemental Material for methods details, valence analysis of another superconducting sample and an insulating bilayer nickelate thin film, SIT analysis, Superconductor-insulator transition (SIT) in another superconducting LPNO thin film, Polarization dependent XAS of Ni L_2 edge and O K edge in another superconducting film, total electron yield (TEY) configuration for XAS and XLD measurements, Raw data of Polarization dependent XAS of Ni L_2 edge and O K edge.
- [47] S. Eley *et al.*, Nat. Phys. **8**, 59 (2012).
- [48] K. Meng *et al.*, Nat. Nanotechnol. **19**, 932 (2024).
- [49] F. Zhu *et al.*, Nucl. Sci. Tec. **35**, 130 (2024).
- [50] Z. Chen *et al.*, Science **373**, 1235 (2021).
- [51] Y. B. Liu *et al.*, Phys. Rev. Lett. **131**, 236002 (2023).
- [52] Y. Wang *et al.*, arXiv:2501.08536 (2025).

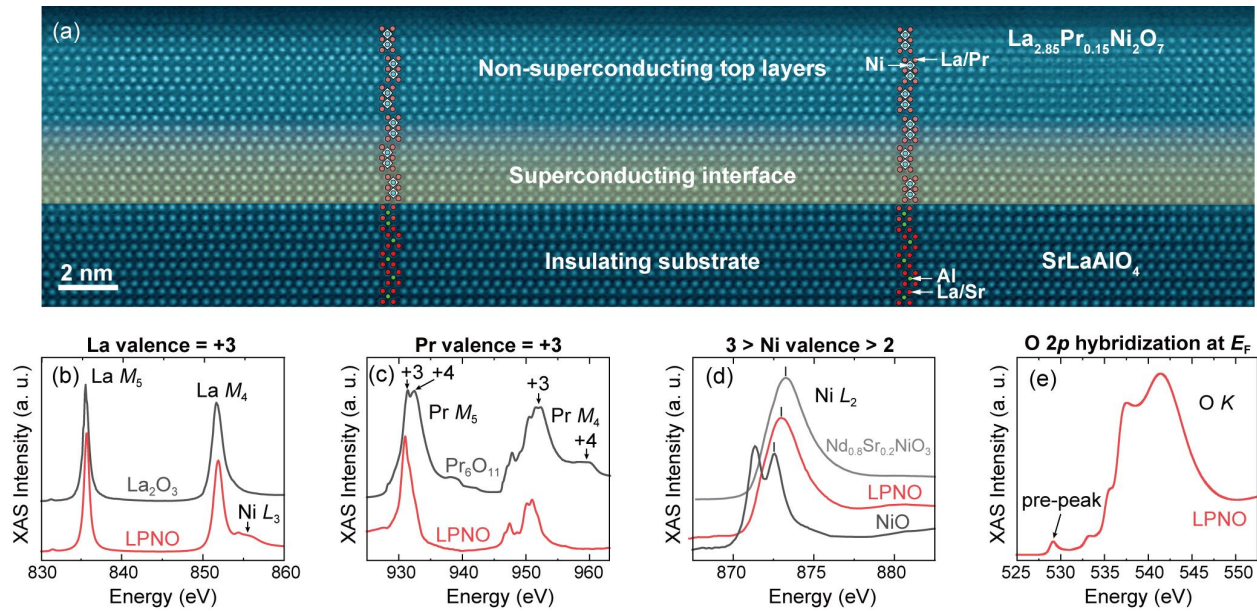


FIG 1. STEM and XAS of superconducting $\text{La}_{2.85}\text{Pr}_{0.15}\text{Ni}_2\text{O}_7$ (LPNO)/ SrLaAlO_4 (SLAO) heterostructures. (a) Extended field view of high-angle annular dark-field (HAADF) image of a 3UC LPNO/SLAO heterostructure. The orange area denotes the superconducting interface. Note that minor damages and defects near the top surface may be partially introduced during focused ion beam (FIB) sample preparation or due to electron beam exposure during measurement. (b) La M_4 and M_5 XAS compared with reference spectra from La_2O_3 . The Ni L_3 edge is visible as a shoulder around 855 eV. (c) Pr M_4 and M_5 XAS compared with reference spectra from Pr_6O_{11} . Arrows indicate the mixed valence states of Pr^{3+} and Pr^{4+} in Pr_6O_{11} . (d) The Ni L_2 XAS compared with reference spectra from NiO and $\text{Nd}_{0.8}\text{Sr}_{0.2}\text{NiO}_3$. The short bar identifies the locations of the peaks. (e) The O K XAS. The pre-peak at 529 eV is indicated by an arrow. XAS measurement temperature is 100 K.

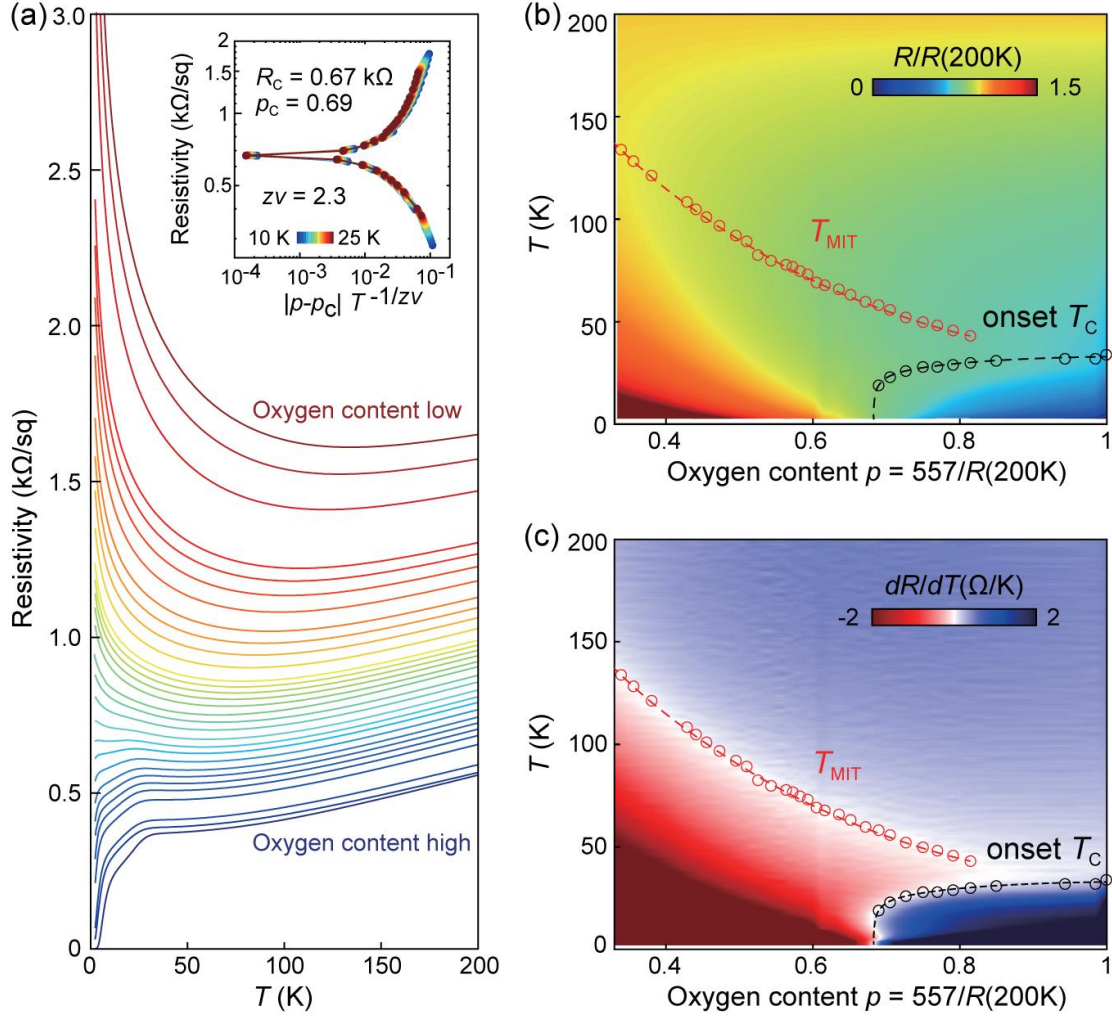


FIG 2. Superconductor-insulator transition (SIT) in the LPNO/SLAO interface. (a) Temperature-dependent resistivity for different oxygen content. The oxygen content, held constant for each curve under 200 K, is systematically adjusted via sequential annealing cycles under 10 Torr helium gas (see supplementary materials). Inset: Finite-size scaling analysis of the SIT within the temperature window from 10 K to 25 K. The oxygen content p is quantified via the empirical relation $p = 557/R(200\text{ K})$. The scaling of resistivity as a function of $|p - p_c|T^{-1/z\nu}$ in the vicinity of the SIT gives an estimated $z\nu$ value of 2.3. (b) Colored mapping of resistivity in the temperature-oxygen content phase diagram. The resistivity at each specified oxygen content is normalized relative to its corresponding value at 200 K. The black circles denote the onset T_C at each p and red circles marks the metal-insulator transition temperature T_{MIT} . (c) Colored mapping of the differential resistivity (dR/dT), with T_{MIT} and onset T_C boundaries delineated.

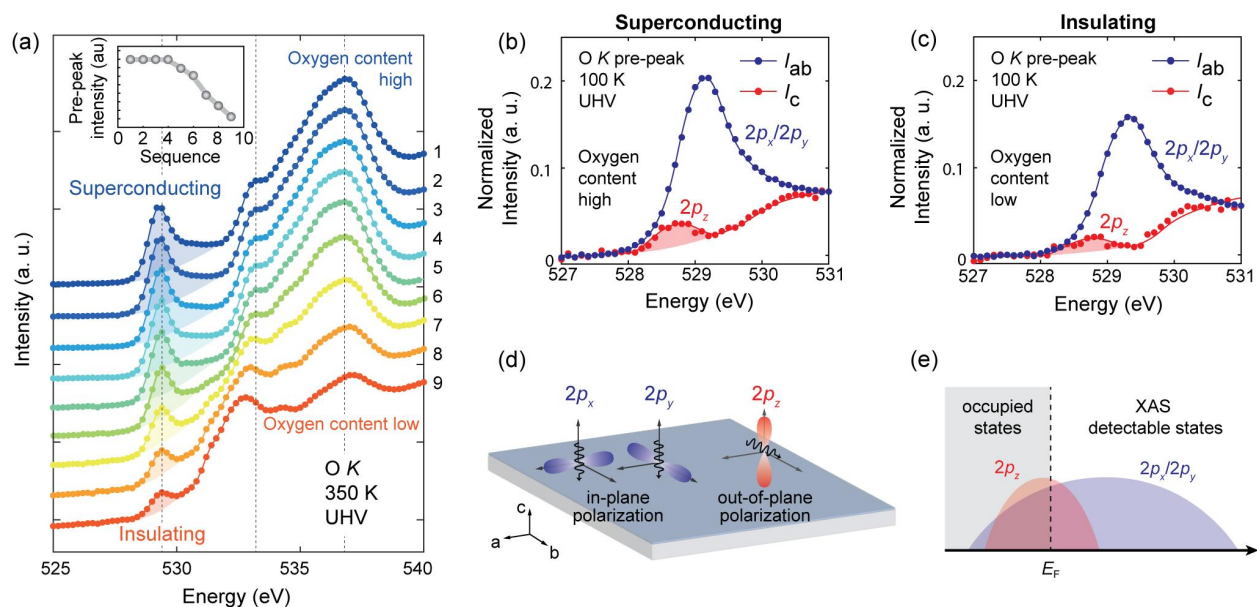


FIG 3. Oxygen orbital electronic structures. (a) XAS of the O K edge during continuous oxygen loss in ultra-high vacuum (UHV) at 350 K. Inset: The pre-peak intensity area integral decreases as the superconducting state with high oxygen content transitions to the insulating state with low oxygen content. (b) and (c) In-plane polarized absorption I_{ab} and out-of-plane polarized absorption I_c around O K pre-peak in the superconducting state and insulating state, respectively. Measurement temperature is 100 K under UHV. (d) Schematic diagram of the XLD measurement. (e) Schematic diagram of the electronic structure of the oxygen $2p$ orbitals.

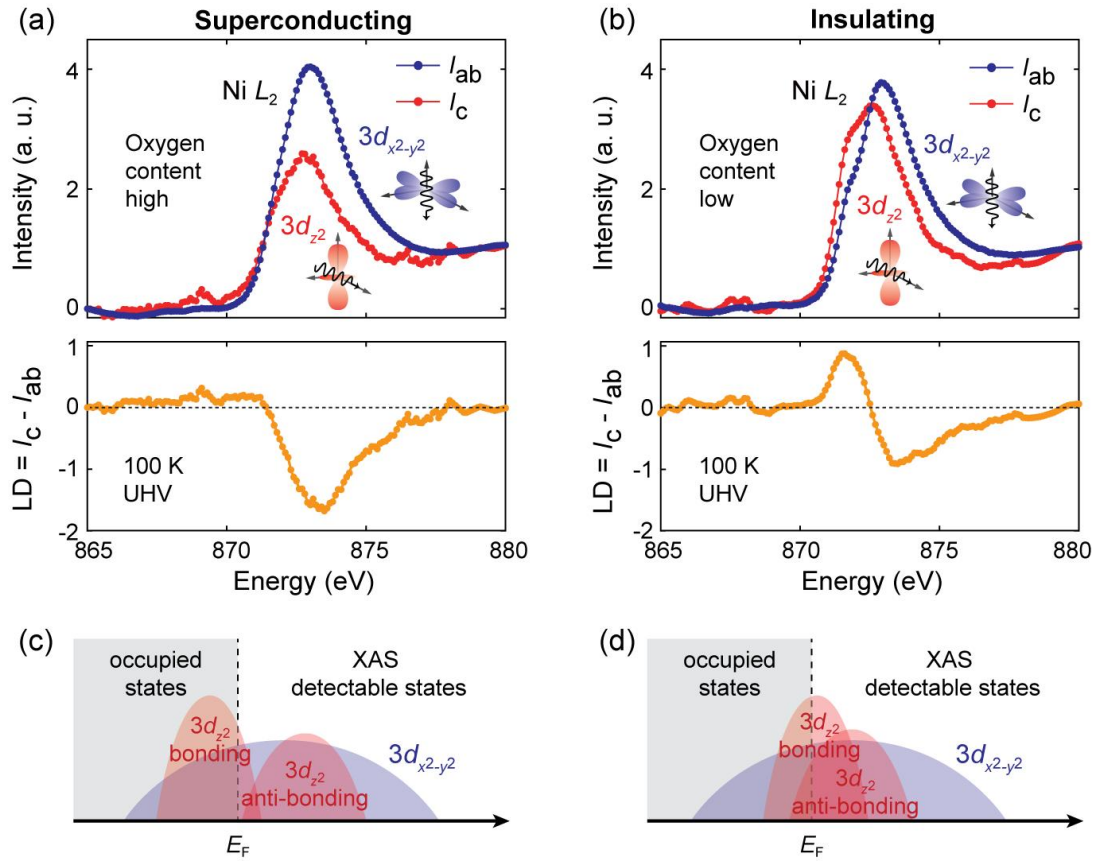


FIG 4. Ni orbital electronic structures. (a) and (b) Polarization dependent XAS of Ni L_2 edge and linear dichroism (LD) signal in the superconducting state and the insulating state, respectively. (c) and (d) Schematic diagram of the electronic structures of the Ni 3d orbitals in the superconducting state and the insulating state, respectively.

Supplementary Materials

Electronic Structures across the Superconductor-Insulator Transition at $\text{La}_{2.85}\text{Pr}_{0.15}\text{Ni}_2\text{O}_7/\text{SrLaAlO}_4$ Interfaces

Heng Wang^{1†}, Haoliang Huang^{1,2†*}, Guangdi Zhou^{1†}, Wei Lv¹, Changming Yue^{1,2,3}, Lizhi Xu¹,
Xianfeng Wu¹, Zihao Nie¹, Yaqi Chen¹, Yu-Jie Sun^{1,2}, Weiqiang Chen^{1,2}, Hongtao Yuan⁴, Zhuoyu
Chen^{1,2*}, Qi-Kun Xue^{1,2,5*}

¹*Department of Physics and Guangdong Basic Research Center of Excellence for Quantum
Science, Southern University of Science and Technology, Shenzhen 518055, China*

²*Quantum Science Center of Guangdong-Hong Kong-Macao Greater Bay Area, Shenzhen
518045, China*

³*Guangdong Provincial Key Laboratory of Advanced Thermoelectric Materials and Device
Physics, Southern University of Science and Technology, Shenzhen, 518055, China*

⁴*National Laboratory of Solid State Microstructures, College of Engineering and Applied
Sciences, Nanjing University, Nanjing, China.*

⁵*Department of Physics, Tsinghua University, Beijing 100084, China*

Methods

Growth. High quality $\text{La}_{2.85}\text{Pr}_{0.15}\text{Ni}_2\text{O}_7$ thin films were grown using the Gigantic-Oxidative Atomic-Layer-by-Layer Epitaxy (GOALL-Epitaxy). The films were grown at a temperature of $\sim 750^\circ\text{C}$, with a laser fluence between 1.4 and 1.8 J/cm^2 . To optimize superconductivity, the as-grown samples were subjected to post-annealing at 575°C for 30 min within the growth chamber, under an atmosphere of purified ozone at a pressure of $\sim 15 \text{ Pa}$ (flow rate $\sim 10 \text{ sccm}$).

Scanning transmission electron microscopy (STEM). High-angle annular dark field (HAADF) imaging of superconducting $\text{La}_{2.85}\text{Pr}_{0.15}\text{Ni}_2\text{O}_7$ was performed using a FEI Titan Themis G2 at 200 kV. The microscope is equipped with a double spherical-aberration corrector (DCOR) and a high-brightness field-emission gun (X-FEG) with a monochromator to enhance image resolution and contrast. The inner and outer collection angles (β_1 and β_2) for HAADF imaging were 90 and 200 mrad, respectively, with a semi-convergence angle of 25 mrad. The beam current was adjusted to about 40 pA to optimize imaging conditions. Cross-section STEM specimens were prepared using a FEI Helios 600i dual-beam FIB/scanning electron microscope (SEM). Prior to extraction and thinning, the sample surface was protected using electron beam-deposited platinum and ion beam-deposited

carbon to prevent ion beam damage. All operations were conducted at room temperature.

Synchrotron soft X-ray absorption spectroscopy (XAS). The XAS measurements were performed at the BL07U beamline at the Shanghai Synchrotron Radiation Facility (SSRF). Prior to loading the sample into the beam endstation, the samples were sealed in an oxygen-preservation container to minimize oxygen desorption during transport. Immediately after decapsulation, the samples were rapidly mounted to a pre-aligned sample holder and transferred into the pre-cooled (100 K) sample manipulator in the XAS measurement chamber.

All XAS spectra were collected in the total electron yield (TEY) configuration with an X-ray normal incident on the sample surface. These XAS were normalized such that the intensity at the pre-edge was set to 0 and the intensity at the post-edge was set to 1. Owing to the vicinity of the strong La M_4 lines, the Ni L_3 line is only visible as a shoulder around 855 eV, but the Ni L_2 line is distinctly observed at 872 eV.

The X-ray linear dichroism (XLD) was measured using polarized incident light at angles of incidence of $\theta = 90^\circ$ and 30° (i.e. I_{90° and I_{30° as depicted in Fig. S5). The absorption with in-plane polarization $I_{ab} = I_{90^\circ}$. The out-of-plane absorption $I_c = [I_{30}$

$- I_{90^\circ \sin^2 \theta} / \cos^2 \theta$. Fig. S6 shows Raw data of polarization dependent XAS of Ni L_2 edge and O K edge .

Oxygen content control. In a Physical Property Measurement System (PPMS) under a vacuum environment (~ 10 Torr helium gas), above 200 K, a progressive resistance increase was observed, attributed to spontaneous oxygen loss from the lattice. To systematically tune oxygen content, samples were held at controlled temperatures (330 K or 350 K) for 15-minute intervals, enabling incremental oxygen desorption. This protocol generated a controlled continuous oxygen deficiency, as evidenced by the persistent resistance rise at 200 K and the concomitant emergence of a superconductor-insulator transition at lower temperatures. The oxygen-dependent electronic phase diagram was thereby reconstructed through this thermochemical modulation approach.

At the synchrotron XAS endstation, the oxygen content within the sample was maintained at lower temperatures (i.e. < 200 K), and modulated at elevated temperatures (e.g., 350 K) under ultra-high vacuum conditions. To elucidate the impact of oxygen loss on the electronic structure, the sample was held at 350 K in ultra-high vacuum, prompting continuous oxygen desorption from the film and inducing a transition from the superconducting to the insulating state. Throughout

this process, changes in the oxygen *K*-edge XAS spectra were monitored to track the evolution of the electronic structure.

Transport measurements. Electric transport measurements were performed using a Physical property measurement system (PPMS) with the temperature in the range of 1.8 K – 400 K. Transport measurements were measured in standard Hall bar geometry through the standard lock-in technique with an AC current of 5 μ A (13 Hz). Hall bar electrodes with Pt were evaporated by magnetron sputtering with a prepatterned hard shadow mask. Samples were found to show an apparent resistance increase in the sample space of PPMS (rough vacuum: 10 torr helium gas) when the temperature is above 200 K, which could be attribute to spontaneous oxygen loss. The lattice structure shows no noticeable difference before and after the oxygen loss process, which was characterized by XRD. The spontaneous oxygen loss process allows us to explore the oxygen dependence of superconductivity.

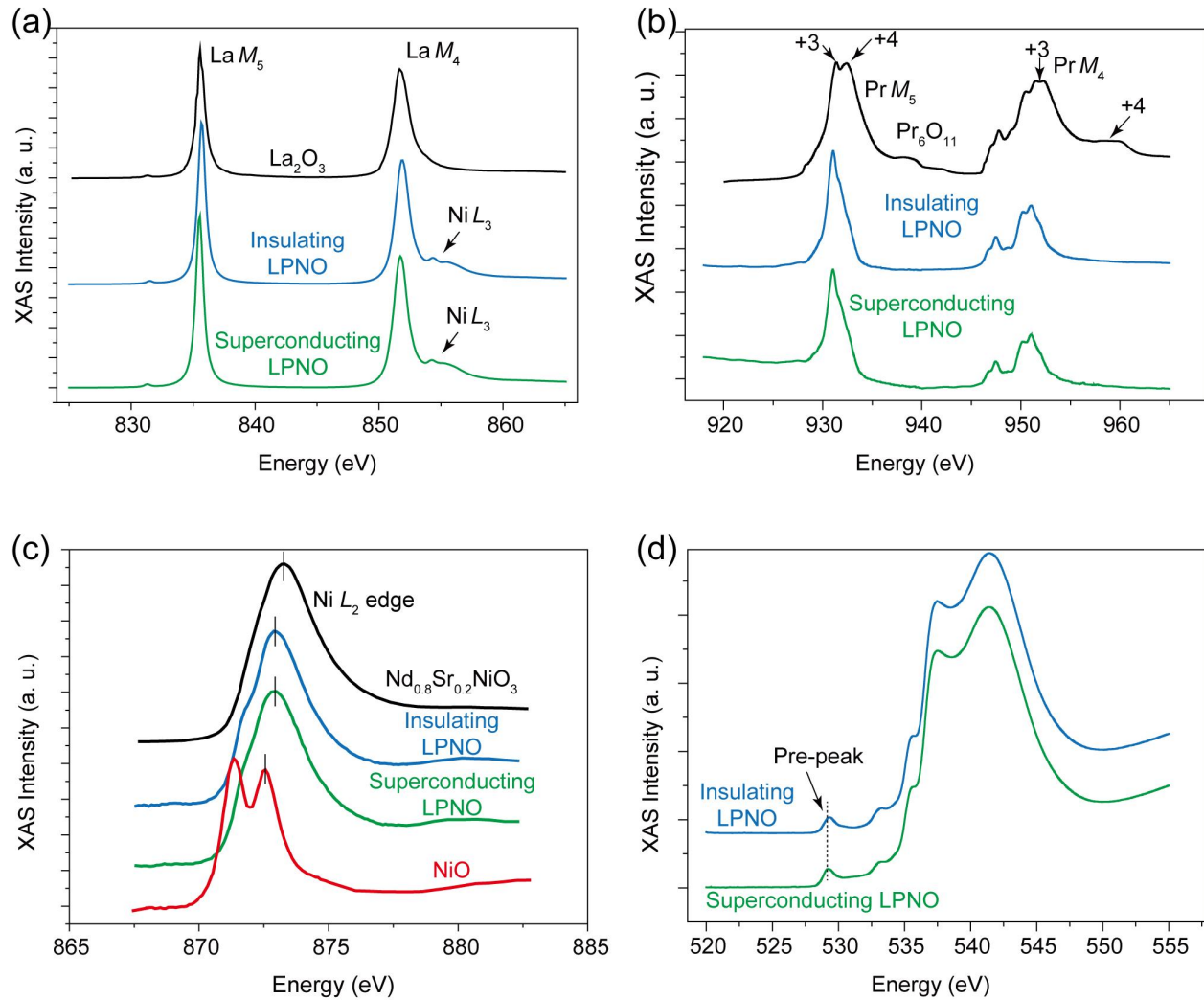


Fig. S1. Valence analysis of another superconducting sample and an insulating bilayer nickelate thin film. (a) La M edge X-ray absorption spectra (XAS) of another superconducting LPNO film and insulating LPNO film compared with reference spectra from La_2O_3 . The Ni L_3 edge is visible as a shoulder around 855 eV. (b) Pr M edge XAS of another superconducting LPNO film and insulating LPNO film compared with reference spectra from Pr_6O_{11} . (c) The Ni L_2 edge XAS of another superconducting LPNO film and insulating LPNO film compared with reference spectra from NiO and $\text{Nd}_{0.8}\text{Sr}_{0.2}\text{NiO}_3$. (d) The O K edge XAS of another superconducting LPNO film and insulating LPNO film.

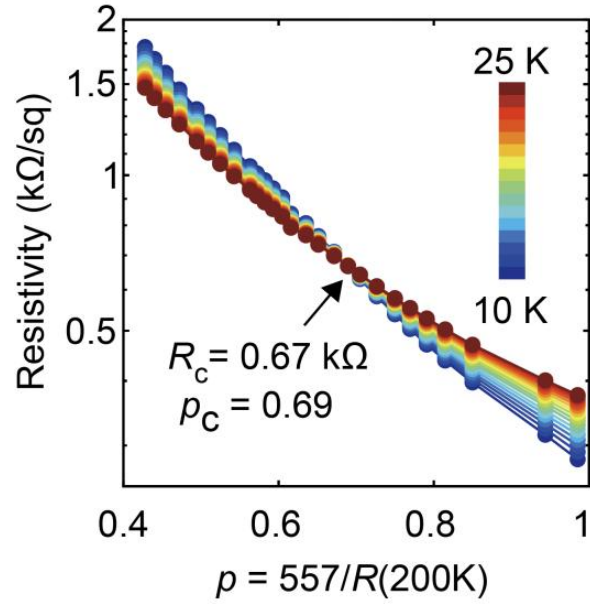


Fig. S2. SIT analysis. Same resistivity data shown in Fig. 2 in the main text, replotted as a function of oxygen content p , zoomed in focusing on the quantum critical region of the SIT. The critical oxygen content p_c is determined to be 0.69, above which the sample shows superconducting transition.

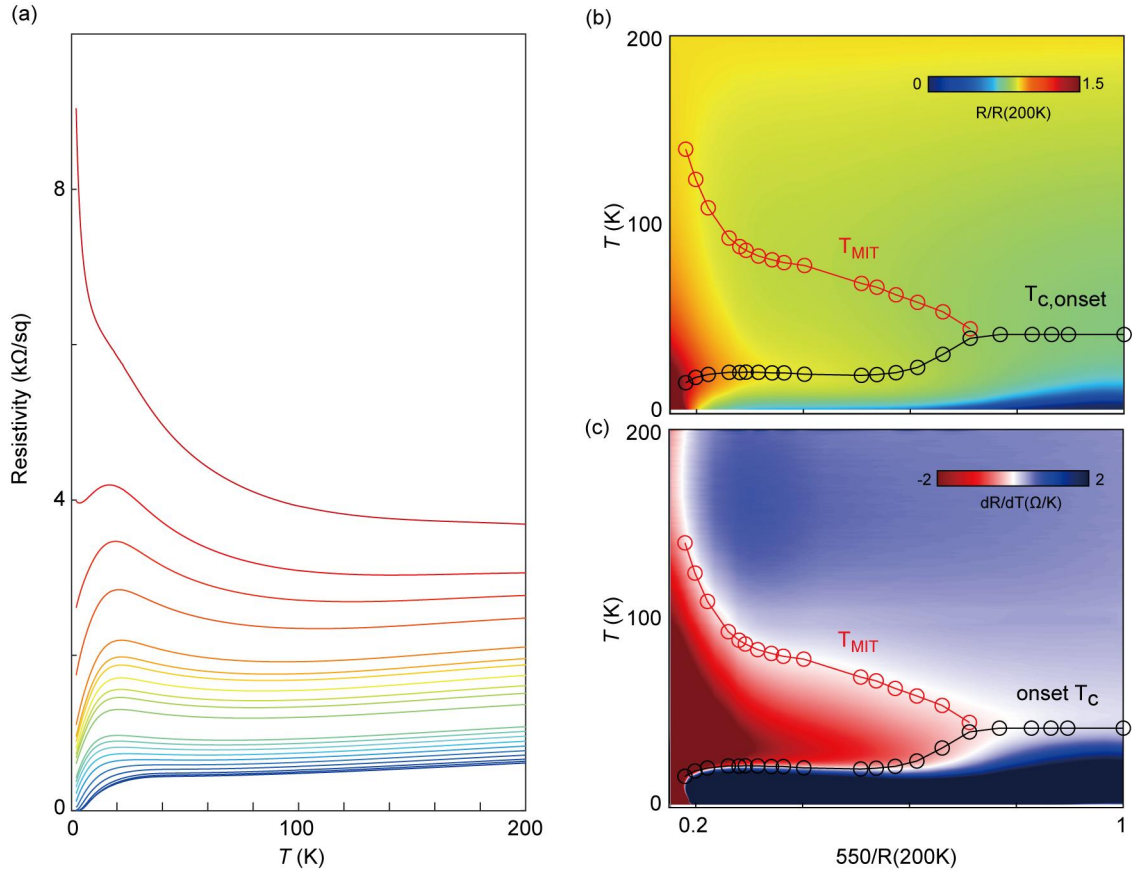


Fig. S3. Superconductor-insulator transition (SIT) in another superconducting LPNO thin film. (a) Temperature-dependent resistivity for different oxygen content. The oxygen content, held constant for each curve under 200 K, is systematically adjusted via sequential annealing cycles (200-380K) under 10 Torr helium gas. (b) Colored mapping of resistivity as a function of temperature and oxygen content. The resistivity at each specified oxygen content is normalized relative to its corresponding value at 200 K. The black circles denote the onset T_C at each p and red circles marks the metal-to-insulator transition temperature T_{MIT} . (c) Colored mapping of the differential resistivity (dR/dT), with T_{MIT} and onset T_C boundaries explicitly delineated.

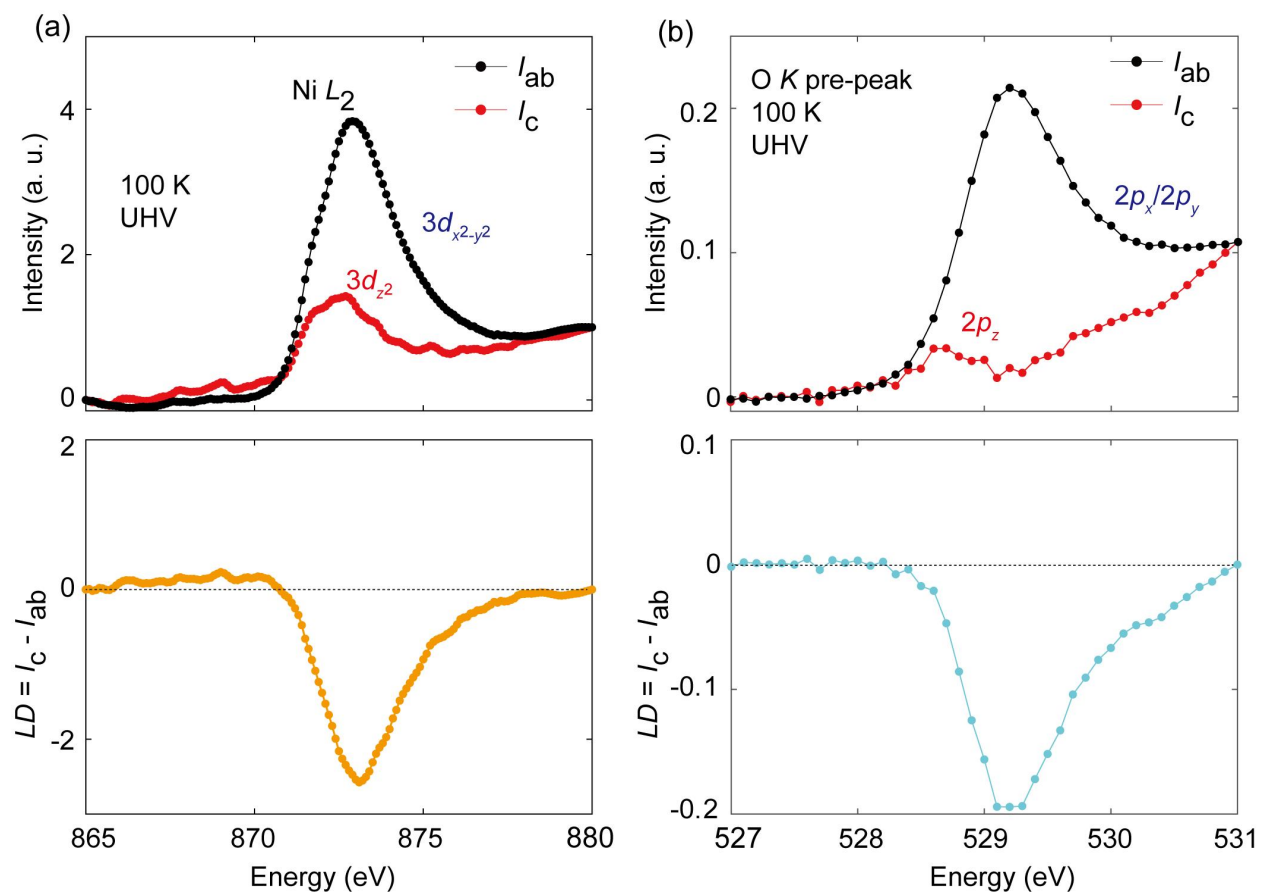


Fig. S4. Polarization dependent XAS of Ni L_2 edge and O K edge in another superconducting film. (a) Top: In-plane polarized absorption $I(ab)$ and out-of-plane polarized absorption $I(c)$ around Ni L_2 edge. Down: Linear dichroism (LD) signal around Ni L_2 edge in the superconducting film. (b) Top: In-plane polarized absorption $I(ab)$ and out-of-plane polarized absorption $I(c)$ around O K pre-peak. Down: Linear dichroism (LD) signal around O K edge in the superconducting film.

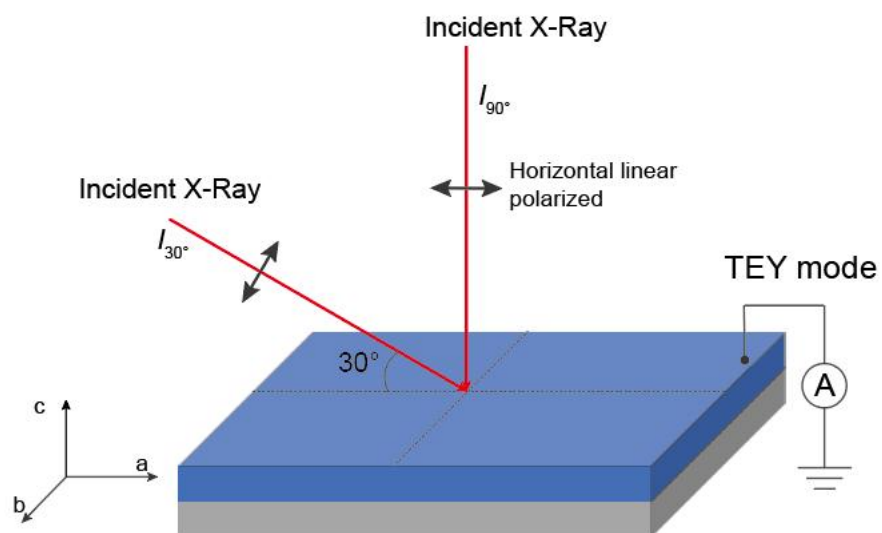


Fig. S5. Total electron yield (TEY) configuration for XAS and XLD measurements.

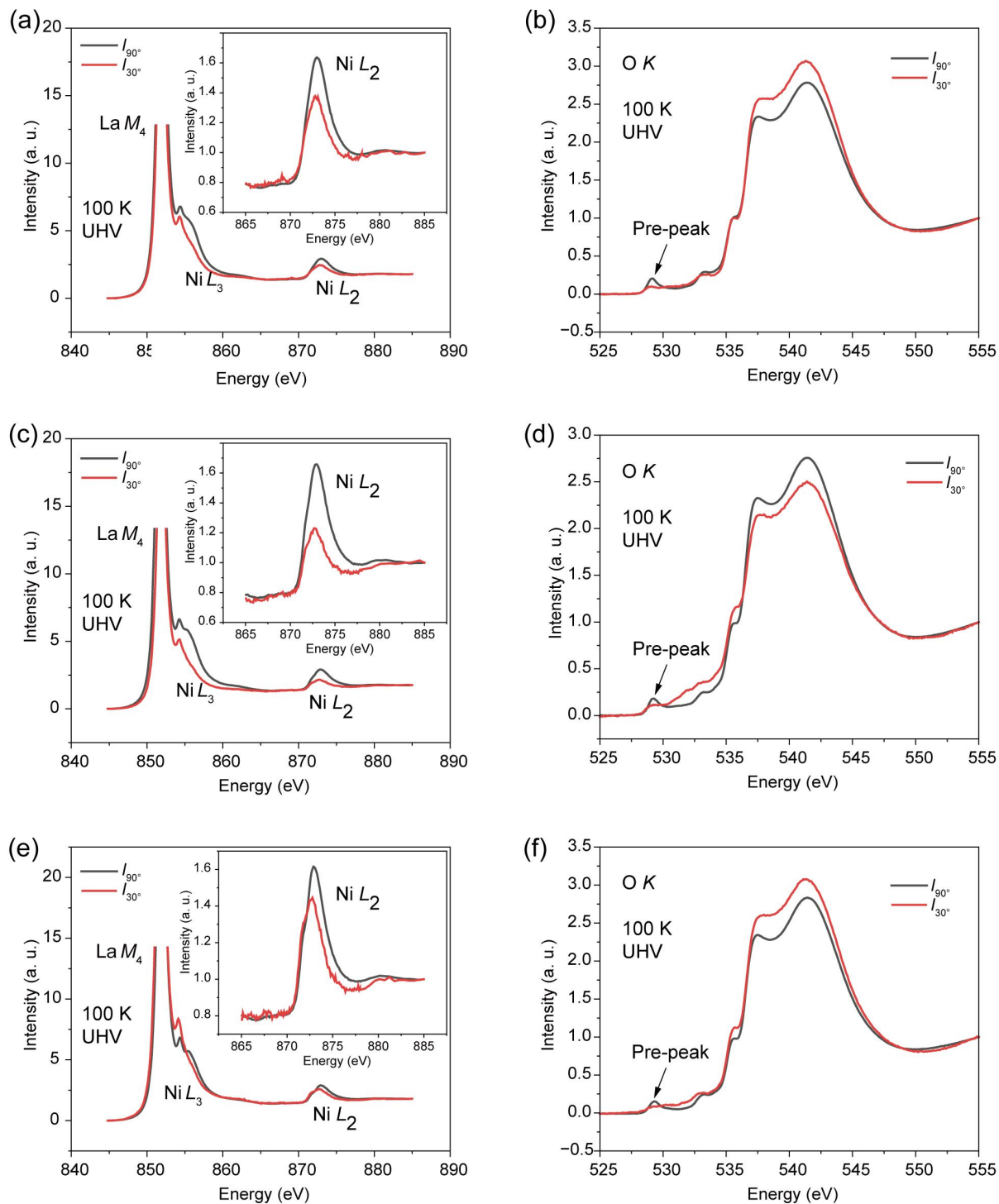


Fig. S6. Raw data of Polarization dependent XAS of Ni L_2 edge and O K edge. (a) and (b) The thin film of the superconducting state described in the main text. (c) and (d) Another thin film in the superconducting state. (e) and (f) The thin film in the insulating state. La M_4 peak was truncated to highlight the signals of Ni.